AERODYNAMIC EFFICIENCY OF HIGH MANEUVERABLE AIRCRAFT APPLYING ADAPTIVE WING TRAILING EDGE SECTION

Christian Breitsamter

Institute for Fluid Mechanics, Aerodynamics Division, Technische Universität München
Boltzmannstrasse 15, 85748 Garching, Germany

Keywords: *Adaptive wing, high agility aircraft, high angle of attack, force measurements*

Abstract

The aerodynamic characteristics of a high-agility aircraft of canard-delta wing type are analyzed in detail comparing the performance obtained by smooth, variable camber wing trailing-edge sections versus conventional trailing-edge flaps. Wind tunnel tests are conducted on a detailed model fitted with discrete elements representing the adaptive wing trailing-edge sections. Force and flow field measurements are carried out to study the aerodynamic properties. Lift, drag and pitching moment coefficients are evaluated to assess aerodynamic efficiency and maneuver capabilities. Comparing the data for adaptive and conventional flap configurations, it is shown that smooth, variable camber results in an increase in lift at given angle of attack and in a decrease in drag at given lift coefficient. These benefits hold also for trimmed conditions. They are demonstrated for an angle-of-attack range of −10 to +30 deg, substantiating a significant improvement in flap efficiency for the adaptive wing concept. Thus, the form-variable wing demonstrates a remarkable potential to enhance flight and maneuver performance and to alleviate maneuver loads, respectively.

1 Introduction

The forthcoming demands on safe and efficient flight operations in context of society needs and environmental impacts enforce continuous improvement of the performance of both civil and military aircraft. A key issue enhancing the aircraft efficiency is the use of advanced and adaptive wing technologies (Fig. 1) [1-4].

The aerodynamic characteristics of adaptive and form-variable wing elements and multifunctional control surfaces have been intensively studied in several German and European research programs [5-8]. Results show increased glide number, reduced drag and improved high lift performance. A main focus is on structural concepts for adaptive flap systems as well as for local surface deformations and the integration of related sensors, actuators and controllers in the aircraft [9]. Local surface thickening known as 'Shock Control Bump' (SCB) is used to modify the shock development at transonic flight conditions [10]. An appropriate position and shape of the SCB may lead to a nearly isentropic recompression along with a reduced pre-shock Mach number. This reduction results in a lower shock strength and, therefore, in a decrease in wave drag. Extensive studies are conducted on the aerodynamic and structural design of SCBs to make them applicable for large transport aircraft wings [11, 12].

Also, advanced structural concepts for variable camber wing trailing-edge sections have been developed. The structural solutions were proven by full scale ground demonstrators applying the so called 'horn concept' [13], the 'girdle concept' [14] and the 'finger concept' [9]. Further studies concentrate on multifunctional control surfaces [15]. For example, small

Copyright © 2004 by C. Breitsamter. Published by the International Council of the Aeronautical Sciences, with permission.
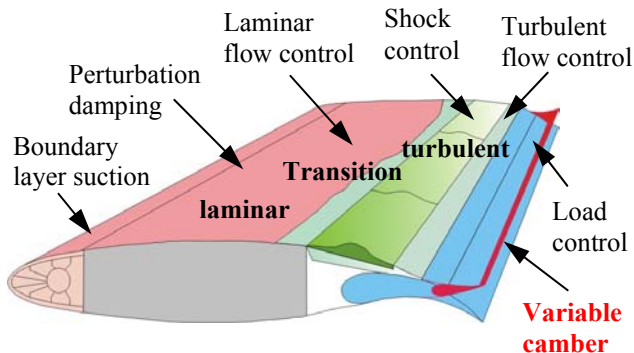
Fig. 1 Adaptive wing technologies.

control surfaces mounted at the trailing-edge of conventional flaps show an increase in maximum lift of about 7% [16]. Recently, investigations on 'Miniature Trailing Edge Devices' (Mini-TEDs) have been performed in wind tunnel and flight tests within the technology platform AWIATOR ('Aircraft WIng with Advanced Technology OpeRation') funded by the European Commission [8].

Concerning military aircraft, comprehensive flight tests were carried out on the F-111 research aircraft to develop and assess the technology enhancements of the 'Mission Adaptive Wing' (MAW), employing smooth contour, variable camber leading- and trailing-edge surfaces [17]. Flight tests were conducted in frame of the joint U.S. Air Force/NASA/ Boeing Advanced Fighter Technology Integration (AFTI/ F-111) program. Improvements in glide number, large reductions in drag at off-design conditions and alleviation of maneuver loads have been successfully demonstrated [18-20].

However, there is a lack of investigations applying adaptive leading- and trailing-edge surfaces on high-maneuverable aircraft fitted with slender wing geometry [21]. Research activities concentrate mainly on related structural concepts but there is also a need for systematic aerodynamic investigations. Therefore, the present study uses an aircraft model of canard-delta wing type to assess the aerodynamic performance of adaptive wing sections versus conventional trailing-edge flaps.

2 Experiment and Test Program

2.1 Model and Facility

Experiments are performed on an 1:15 scaled detailed steel model of a modern high-agility aircraft (Fig. 2). Major parts of the model are nose section, front fuselage with rotatable canards and a single place canopy, center fuselage with delta wing and a through-flow double air intake underneath, and rear fuselage including nozzle section and empennage (fin). The baseline wing configuration is equipped with conventional inboard and outboard trailing-edge flaps. The model elements designed to represent the smooth, variable camber of the adaptive wing trailing-edge section have the same spanwise and chordwise dimensions as the conventional flaps. The form-variable section is composed by six discrete wing elements which are exchanged for the conventional flaps to run the adaptive wing tests. The corresponding deflections are defined by the tangent on the trailing-edge including values of η_{FT} = 0°, 5°, 10°, 15°, 20°, and 25° (Fig. 3). To evaluate the aerodynamic performance obtained by adaptive wing versus conventional flaps, the comparison is based on a measure of deflection angles with respect to the skeleton line. Fig. 4 depicts the corresponding definitions used for conventional flap deflection η_K and deflection of the form-variable trailing-edge section η_{FS}.

The experiments have been carried out in the large low-speed facility A of the Institute for Fluid Mechanics (Aerodynamics Division) of Technische Universität München. This closed-return wind tunnel can be operated with both open and closed test section at maximum usable velocities of 75 *m/s* and 65 *m/s*, respectively. Test section dimensions are 1.8 *m* in height, 2.4 *m* in width and 4.8 *m* in length. Because high angle-of-attack experiments are conducted the open test section is used. The test section flow was carefully inspected and calibrated documenting a turbulence level less than 0.4% and uncertainties in the spatial and temporal mean velocity distributions of less than 0.067%.

$2s$	$= 0.740$ m	$\varphi_W = 50°$	Index:
l_μ	$= 0.360$ m	$\varphi_W = 45°$	W: Wing
AR_W	$= 2.45$	$\lambda_W = 0.14$	C: Canard
AR_F	$= 1.38$	$\varphi_F = 54°$	F: Fin
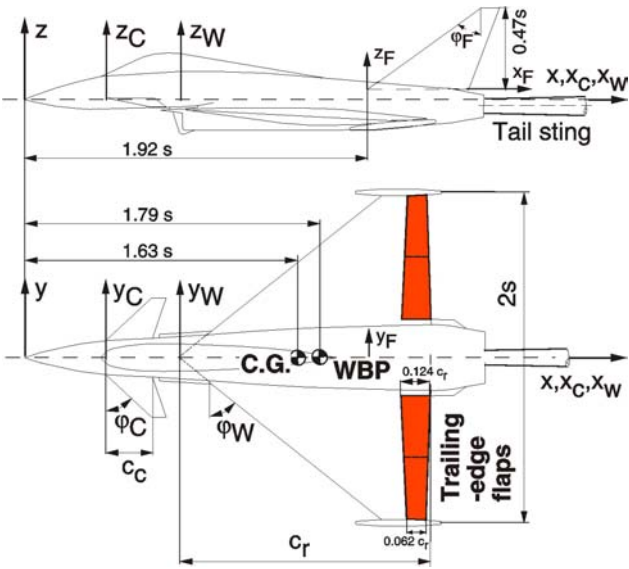
Fig. 2 Model geometry of delta-canard fighter aircraft.

Fig. 3 Wing trailing-edge elements representing the smooth contour, variable camber trailing-edge section.
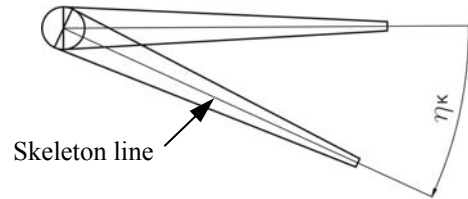
a) Conventional trailing-edge flap.
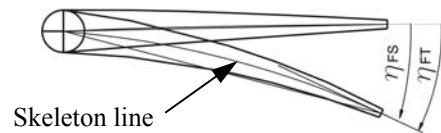
b) Form-variable trailing-edge section.

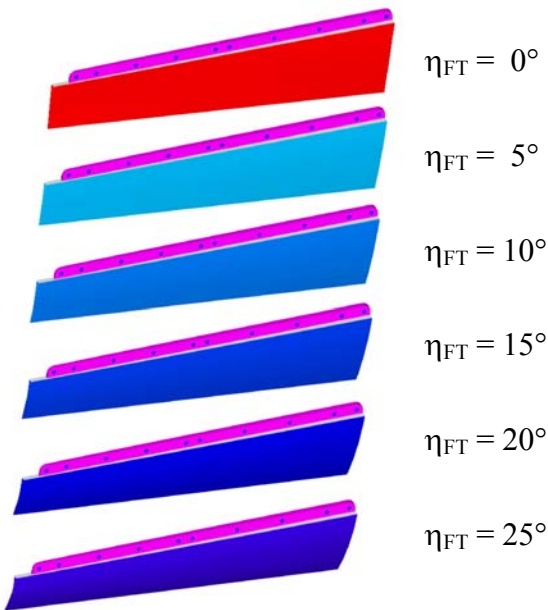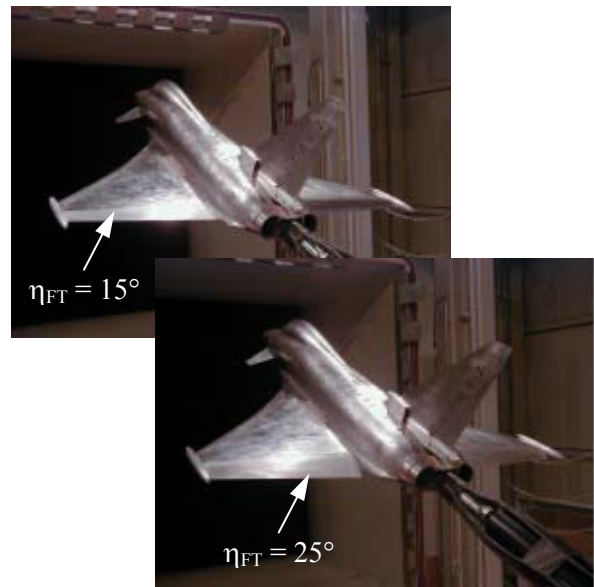**Fig. 4** Definition of trailing-edge deflections.

a) Front view.

b) Rear views.

Fig. 5 Model mounted in test section.

Fig. 6 Components for strain gauge balance integration and connection with tail sting adapter.
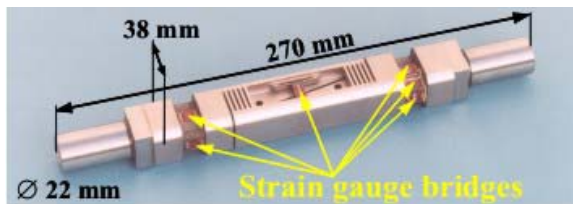

Fig. 7 Six-component strain gauge balance.

The model is sting mounted using a specific tail sting with its left cylinder attached to the internal strain gauge balance and its right conical part connected with the horizontal sting of the 3-axis model support (Figs. 5 and 6). The computer controlled model support provides an angle-of-attack range of $-10° \leq \alpha \leq +30°$, and models may be yawed and rolled 360°. The uncertainty in angle setting is less than 0.05°.

2.2 Force Measurements

An internal six-component strain gauge balance is used to measure aerodynamic forces and moments (Fig. 7). This strain gauge balance was designed and fabricated at the Technical University of Darmstadt. It is manufactured from one piece of Maraging steel 250 (1.6359). Side and normal forces as well as pitching and yawing moments are measured at corresponding lateral/vertical bending positions close to the balance end cylinders. The axial force is measured using an axial bending station and the rolling moment is obtained by a parallelogram spring. All six measurement stations are equipped with advanced, self temperature compensating strain

gauge bridges. The balance is designed to sustain maximum loads of 900 *N*, 450 *N*, and 2500 *N* for axial, lateral and normal forces, respectively, and maximum moments of 120 *Nm*, 160 *Nm*, and 120 *Nm* for rolling, pitching, and yawing moments, respectively. The accuracy based on maximum loads ranges from 0.05% to 0.1% for the force components and from 0.8% to 1.2% for the moment components. The strain gauge bridges are connected with six-wire conductors to the carrier frequency amplifier modules of a specific measurement system (HBM MGC plus). This system is fully computer controlled providing also the excitation for the strain gauge bridges.

The calculation of forces and moments from the balance signals employs a comprehensive balance calibration. The mathematical relationship assigning balance signals to given loads uses a third order approximation of the balance behavior. Pure single loads and combinations of single loads are stepwise applied to the balance during the calibration. The evaluation of each loading sequence is based on a least square error second order polynomial approximation. The complete calibration coefficient matrix is derived from those evaluations resulting in a system of equations. The related solution applies a least square error method to obtain the aerodynamic loads from the balance signals [22].

2.3 Test Conditions and Data Processing

Force measurements have been made at free stream reference velocities of $U_\infty = 40$ *m/s* and $U_\infty = 60$ *m/s* at ambient pressure p$_\infty$ and ambient temperature T$_\infty$. The corresponding Reynolds numbers based on the wing mean aerodynamic chord are $Re_{l\mu} = 0.97$ x 10^6 and 1.46 x 10^6, respectively. Thus, turbulent boundary layers are present at wing and control surfaces. The angle of attack is varied in the range of $-10° \leq \alpha \leq +30°$ with steps of $\Delta\alpha = 2°$. Canard and leading-edge control surfaces are set to 0°. The conventional trailing-edge flaps are deployed at $\eta_K =$ 0°, 5°, 10°, 15°, 20°, and 30°, and adaptive trailing-edge deflections are set to $\eta_{FT} = 0°$, 5°, 10°, 15°, 20°, and 25°. Prior to the angle-of-attack tests at wind-on conditions, a polar at

wind-off is conducted for each model configuration. The associated loads caused by mass forces (model weight) are subtracted from the total measured loads to obtain aerodynamic forces and moments only. Sting influence is considered as well.

The voltages of the strain gauge bridges are amplified for optimal signal level and simultaneously sampled at 15 *Hz* and digitized with 16 bit precision. The sampling interval is 33.33 *s*, thus providing a sample block of 500 discrete values for each point of the angle-of-attack polar. Based on that samples mean values of aerodynamic forces (lift *L*, drag *D*, side force *Y*) and moments (pitching moment *m*, rolling moment *l*, yawing moment *n*) are calculated. Moments are related to the balance reference point WBP (Fig. 2). The corresponding aerodynamic coefficients C_L, C_D, C_Y, C_m, C_l, and C_n are referred to dynamic free stream pressure $q_\infty = (\rho_\infty/2)\,U_\infty^2$ (density $\rho_\infty = f(T_\infty, p_\infty)$), wing area A_W and wing mean aerodynamic chord l_μ and wing semi span s, respectively. Here, the coefficients associated with the longitudinal motion are discussed:

$$C_L = L\,/(\,q_\infty\,A_W\,) \qquad (1)$$

$$C_D = D\,/(\,q_\infty\,A_W\,) \qquad (2)$$

$$C_m = m\,/(\,q_\infty\,A_W\,l_\mu) \qquad (3)$$

Flap efficiencies due to changes in lift and pitching moment are given by the following derivatives (*j = K, FS*):

$$C_{L\eta j} = dC_{Lj}\,/d\eta_j \qquad (4)$$

$$C_{m\eta j} = dC_{mj}\,/d\eta_j \qquad (5)$$

3 Results and Discussion

3.1 Preparatory Tests

The accuracy of the complete measurement system has been carefully tested. Results of the lift coefficient as function of angle of attack show a perfect agreement comparing up-stroke and down-stroke angle-of-attack motions (Fig. 8).

This agreement is also true for the other aerodynamic coefficients substantiating correct and stiff linkages between tail sting, balance and model. None of the results of repeated measurement runs exceed the balance error levels.

The comparison of lift coefficients for different Reynolds numbers, namely $Re_{l\mu} = 0.97$ x 10^6 ($U_\infty = 40$ *m/s*) and 1.46 x 10^6 ($U_\infty = 60$ *m/s*), indicates no remarkable differences regarding the angle-of-attack range tested (Fig. 9). Similar tendencies are found for all other aerodynamic coefficients. The data show there is no significant Reynolds number effect for that low-speed region because turbulent boundary layers exist and the flow separates at wing leading-edges already at moderate angles of attack. Hence, further results are presented for $U_\infty = 40$ *m/s* only.
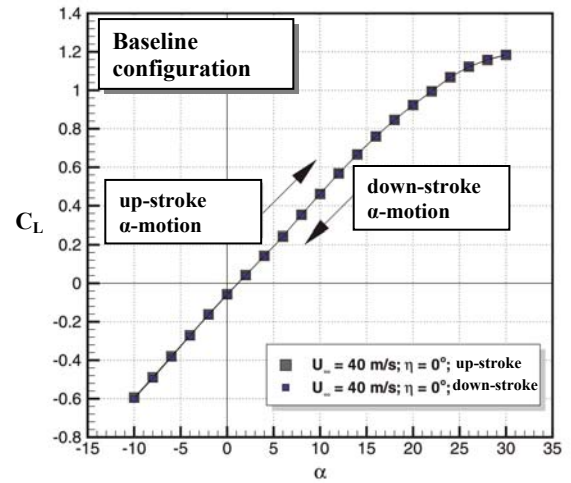

Fig. 8 Lift coefficient as function of angle of attack for up-stroke and down-stroke measurement cycles.
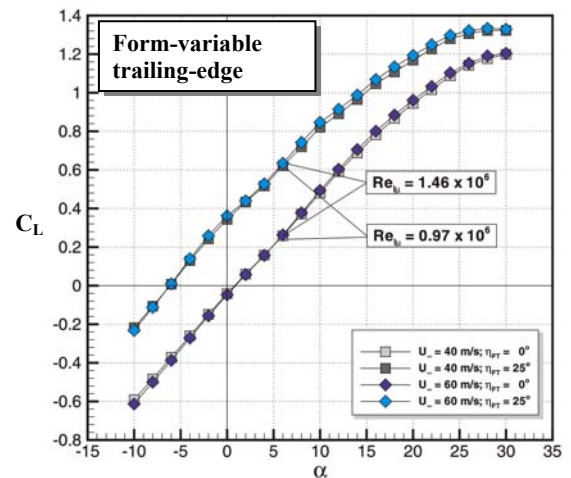

Fig. 9 Lift coefficient as function of angle of attack for different Reynolds numbers $Re_{l\mu}$.

3.2 Flow Field Characteristics

Three main flow field types develop sequentially on the delta wing with increasing angle of attack (Fig. 10; $\eta_{FT} = 0°$). Firstly, the flow is attached on the wing upper surface up to moderate incidences ($\alpha < 4°$). Secondly, at $\alpha \approx 4°$, the flow separates at the delta wing leading-edges with fast transition from bubble- to vortex-type. The roll-up of the separated shear layers starts at the wing tip and progresses to the apex to form a fully developed leading-edge vortex. The leading-edge vortices of the delta wing port and starboard side induce velocities in planes normal to the free stream direction producing pronounced suction peaks in the wing upper surface pressures. This suction evokes a non-linear increase in lift. The present wing geometry generate leading-edge vortices of moderate strength because the wing sweep is also moderate ($\varphi_w = 50°$). Therefore, the non-linear part, evident in the lift curve above $\alpha > 6°$, is small. With further increasing incidence the vortex rotational core grow and vortex trajectories are shifted inboard and upward. Thirdly, an abrupt change in the vortex core structure well known as vortex bursting/breakdown occurs at a certain high angle of attack [23]. This phenomenon is due to the rise in the adverse pressure gradient with increasing angle of attack. The rise in core static pressure causes stagnation of the axial core flow

and thus, a sudden expansion of the vortex core takes place. Vortex breakdown is linked to the transition from stable to unstable core flow evident by the change from jet-type to wake-type axial velocity profiles. This transition is accompanied by maximum turbulence intensities at the breakdown position and increased turbulence levels in the breakdown wake. Here, vortex bursting for the baseline configuration ($\eta_{FT} = 0°$) occurs at the delta wing trailing-edge at $\alpha \approx 12°$. At $\alpha = 30°$, vortex bursting is located close to the apex. The maximum lift coefficient C_{Lmax} is also reached at $\alpha \approx 30°$.

3.3 Aerodynamic Characteristics of Adaptive versus Conventional Trailing-Edge Flaps

3.3.1 Lift

The lift coefficient vs. angle of attack is plotted for all form-variable trailing-edge deflections in Fig. 10. It is shown that positive trailing-edge camber ($\eta > 0$) shifts the lift coefficient at zero angle of attack, C_{L0}, to markedly higher values. Further, there is a substantial increase in the maximum lift coefficient C_{Lmax}. However, the increase in lift becomes reduced at high angle-of-attack because downstream of vortex bursting regions of low velocities and irregular flow arise near the surface. Also, regions of separated flow occur at the trailing-edge, especially in the
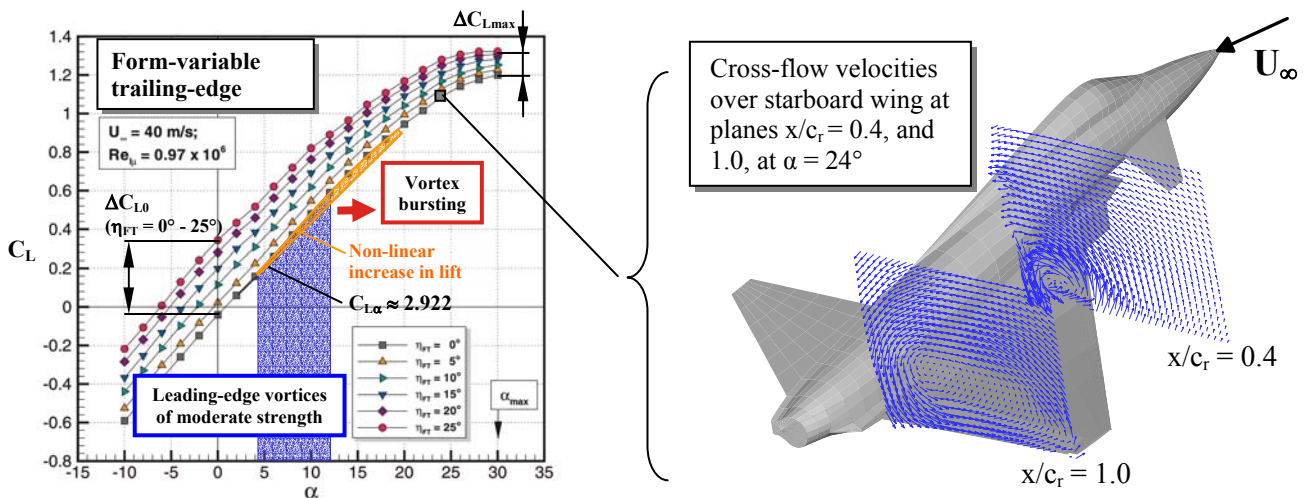

Fig. 10 Lift coefficient as function of angle of attack for the configuration with form-variable trailing-edge section at deflections of $\eta_{FT} = 0°$, 5°, 10°, 15°, 20°, and 25°.
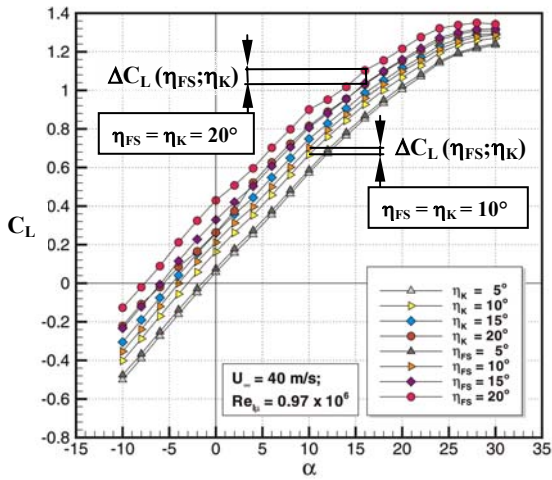
Fig. 11 Lift coefficient as function of angle of attack comparing the configurations with form-variable trailing-edge section vs. conventional flaps deflected at η_{FS}, $\eta_K =$ 5°, 10°, 15°, and 20°.

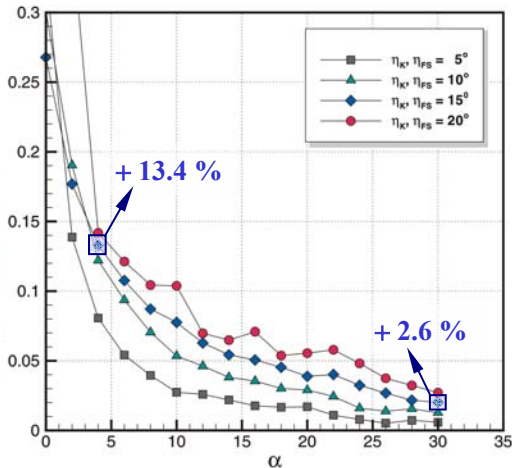$(C_L(\eta_{FS}) - C_L(\eta_K))/ C_L(\eta_K)$ x 100   [%]

Fig. 12 Relative differences in lift coefficient between configurations with form-variable trailing-edge section and conventional flaps as function of angle of attack for η_{FS}, $\eta_K =$ 5°, 10°, 15°, and 20°.

outboard (wing tip) area. Therefore, flap efficiency of conventional outboard flaps is typically lower than that of inboard flaps. To counter his effect an adaptive trailing-edge section will provide a continuous decrease of outboard and increase of inboard deflections at high incidences.

The comparison of data for form-variable vs. conventional flaps shows that smooth, variable camber results in a higher lift coefficient over the whole angle-of-attack range tested (Fig.

11). Even a remarkable increase in maximum lift can be detected for all investigated trailing-edge deflections. The differences in lift coefficient between the configurations with form-variable and conventional trailing-edge flaps increase with flap deflection. The potential of the adaptive wing trailing-edge section in generating more lift is attributed to the smooth, variable camber based on continuously rising contour gradient and curvature. The differences in lift become markedly lower at $\alpha > 22°$ because vortex bursting dominates the overall flow behavior on the wing upper side. Fig. 12 depicts the differences in lift coefficient between the configurations applying form-variable and conventional trailing-edge flaps normalizing the results by the values of the conventional case. For example, the form-variable trailing-edge deflected at $\eta_{FS} = 15°$ provides higher lift of 13.4% to 2.6% in the angle-of-attack range of $4° \leq \alpha \leq 30°$.

3.3.2 Drag
The lift-to-drag (Lilienthal) polars demonstrate a shift in minimum drag coefficient to higher lift coefficients if the trailing-edge flap is deflected (Fig. 13). It reflects the rise in glide number with increasing trailing-edge camber. The results of the form-variable cases indicate a strong reduction in drag at given lift coefficients compared to the data of the conventional flap configuration. The lower drag is mainly caused by an improved drag coefficient at zero lift due to better flow alignment at the smooth, variable camber contour alleviating the separation tendency at the trailing-edge. Relative differences in the drag coefficients between adaptive and conventional flap configurations are plotted in Fig. 14 for $\eta_K = \eta_{FS} = 5°$, and 15°. The relative difference $(C_D(\eta_{FS}) - C_D(\eta_K))/ C_D(\eta_K)$ for $\eta_K = \eta_{FS} = 15°$ is −26.5% at $C_L = 0.4$ and still −9.5% at $C_L = 1.2$. The drag reduction decreases at higher angles of attack as induced drag grows and wing upper flow is largely separated.

Lilienthal polars related to form-variable and conventional cases of trimmed conditions are shown in Fig. 15. A reference center of gravity (c.g., Fig. 2) with respect to an original aircraft is chosen to re-calculate the aerodynamic coefficients. The graphs exhibit again a
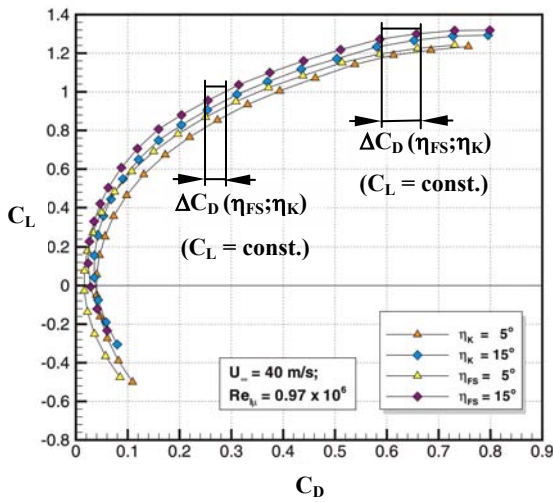
Fig. 13 Lift coefficient as function of drag coefficient comparing the configurations with form-variable trailing-edge section vs. conventional flaps deflected at η_{FS}, η_K = 5°, and 15°.

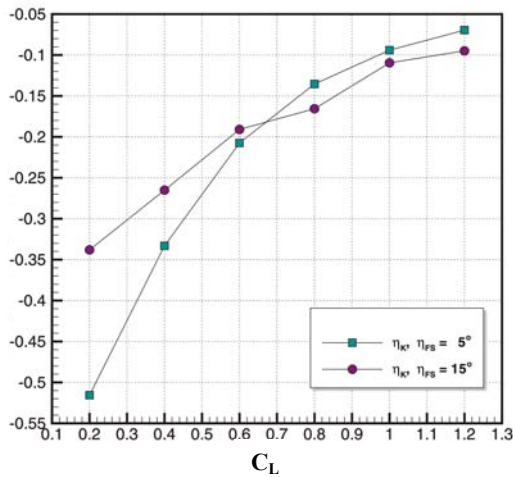$$(C_D(\eta_{FS}) - C_D(\eta_K))/ C_D(\eta_K) \times 100 \quad [\%]$$

Fig. 14 Relative differences in drag coefficient between configurations with form-variable trailing-edge section and conventional flaps as function of lift coefficient for η_{FS}, η_K = 5°, and 15°.

significantly improved lift-to-drag performance applying variable camber trailing-edge section.

3.3.3 Pitching Moment

The nose-up pitching moment increases with angle of attack and lift coefficient, respectively (Fig. 16). The curve of the baseline configuration ($\eta_{FT} = 0°$) exhibits a kink at $\alpha \approx 18°$ indicating a local drop in the nose-up behavior. This kink results from the upstream shift of vortex bursting with increasing angle of attack. Consequently, the amount of lift ahead of the moment
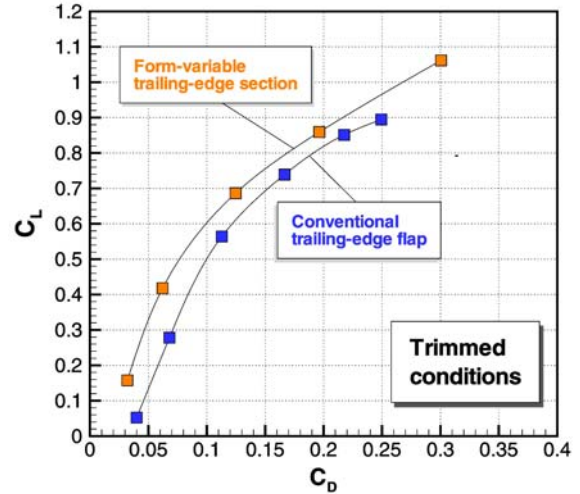

Fig. 15 Lift coefficient as function of drag coefficient for trimmed conditions comparing configurations with form-variable trailing-edge section vs. conventional flaps.
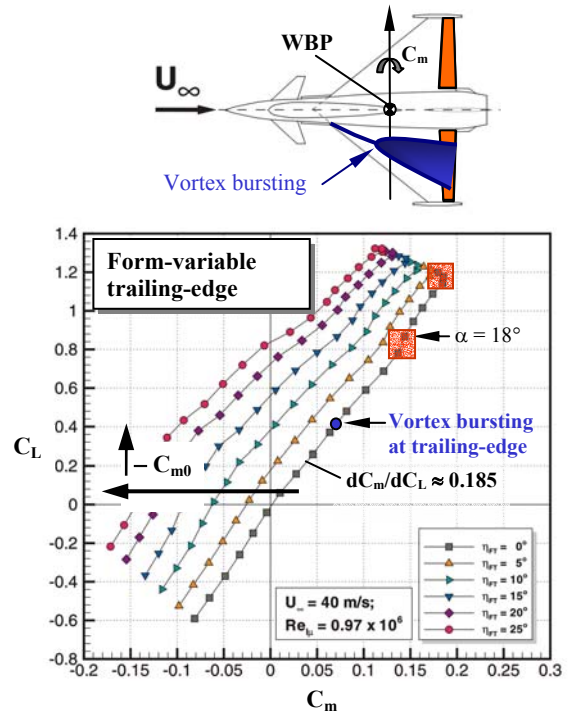

Fig. 16 Lift coefficient as function of pitching moment coefficient for the configuration with form-variable trailing-edge section at deflections of $\eta_{FT} = 0°$, 5°, 10°, 15°, 20°, and 25°.

reference point (WBP) causing a positive pitching moment becomes reduced. Approaching maximum lift, the gradient of pitching moment coefficient related to lift coefficient dC_m/dC_L changes its sign indicating the loss of lift on the wing upper (suction) side.

A positive trailing-edge deflection leads to the typical behavior of an increase in nose-down
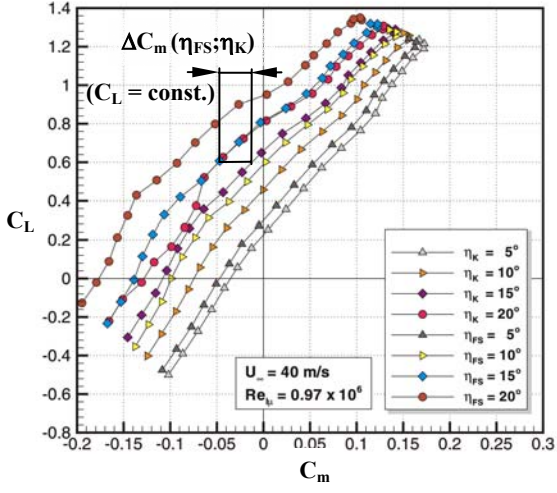
Fig. 17 Lift coefficient as function of pitching moment coefficient comparing the configurations with form-variable trailing-edge section vs. conventional flaps deflected at η_{FS}, η_K = 5°, 10°, 15°, and 20°.

pitching moment, particularly in C_{m0} (Figs. 16 and 17). Compared to the conventional case, the trailing-edge variable camber produces a larger nose-down pitching moment because of higher lift generated in the trailing-edge region. The form-variable configuration is characterized by a quasi linear trend for the rise in the nose-down pitching moment at zero lift, C_{m0}, with deflection angle η_{FT}. This trend can be approximated by the following relationship based on linear potential theory, with x_K denoting the relative position of the variable camber section:

$$C_{m0} = -1.715 \sqrt{(x^3_k (1-x_k))} \, \eta_{FT} \qquad (6)$$

3.3.4 Flap Efficiency

The values of lift coefficient as function of the deflection of conventional trailing-edge flap η_K and form-variable trailing-edge section η_{FS}, respectively, are plotted for several angles of attack in Fig. 18. It is shown that the gradient of the curves, $C_{L\eta}$, is larger for the form-variable cases compared to the associated conventional flap deflections. In particular, increased gradients of $C_{L\eta}$ are evident for both large deflection angles and at high lift coefficients, substantiating an enhanced flap efficiency obtained by adaptive wing geometry. Corresponding characteristics
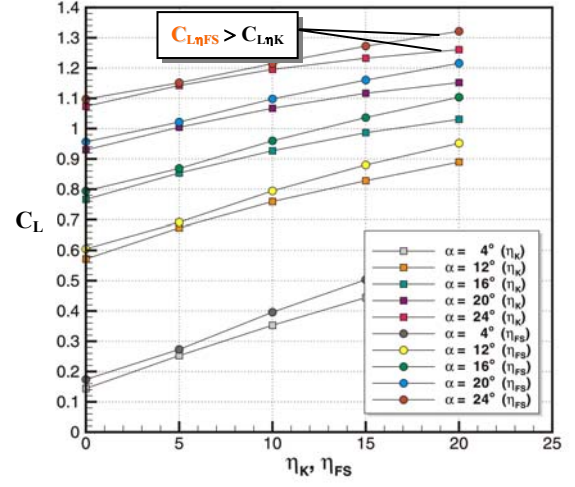

Fig. 18 Lift coefficient as function of deflection angles η_K and η_{FS}, respectively, at several angles of attack.
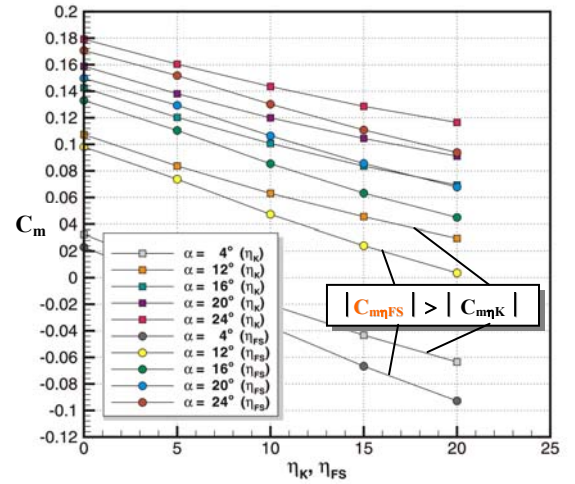

Fig. 19 Pitching moment coefficient as function of deflection angles η_K and η_{FS}, respectively, at several angles of attack.

are found analyzing the pitching moment coefficients as function of the deflection angles (Fig. 19).

For further evaluation, the required form-variable trailing-edge deflections $\eta_{FS\text{-}CL\text{-}eq}$ and $\eta_{FS\text{-}Cm\text{-}eq}$ to achieve equivalent increase in lift and pitching moment, respectively, are computed:

$$\eta_{FS\text{-}CL\text{-}eq} = (C_{L\eta FS})^{-1} \, (C_{L\eta K}) \cdot 1[°] \qquad (7)$$

$$\eta_{FS\text{-}Cm\text{-}eq} = (C_{m\eta FS})^{-1} \, (C_{m\eta K}) \cdot 1[°] \qquad (8)$$
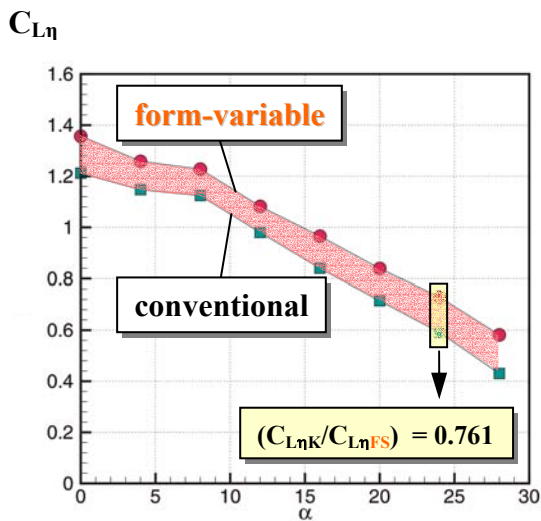
$C_{L\eta}$

Fig. 20 Flap efficiency $C_{L\eta}$ as function of angle of attack comparing configurations with form-variable trailing-edge section vs. conventional flaps.

Improved flap efficiencies of the adaptive wing result in lower trailing-edge deflections $\eta_{FS-CL-eq}$ and $\eta_{FS-Cm-eq}$ with respect to the conventional flap deflections η_K for comparative alteration of lift or pitching moment. For example, the form-variable trailing-edge deflection is only about 75% of the conventional one to obtain an equivalent increase in lift at angle of attack of α = 24° (Fig. 20). The decrease in the gradients $C_{L\eta}$ and $C_{m\eta}$, typically observed for conventional trailing-edge flaps at high angle-of-attack, is markedly lower for the adaptive wing.

3 Conclusions

The aerodynamic characteristics of a high maneuverable aircraft of canard-delta wing type have been intensively investigated focusing on the effectiveness of a form-variable trailing-edge section. Aerodynamic efficiencies related to smooth, variable camber trailing-edge geometry are compared with those achieved with conventional trailing-edge flaps. The comparison of flight and maneuver performance is based on force and flow field measurements. Aerodynamic forces and moments are measured applying an advanced internal six-component strain gauge balance connected to a high accuracy measurement system. To perform the ex-

periments the form-variable trailing-edge section is exchanged for the conventional inboard and outboard flaps. The configurations tested include six discrete elements representing smooth, variable camber contours with trailing-edge deflections in the range of 0° to 25°. Conventional flaps are deflected from 0° to 30°. The comparison of data is based on equivalent deflection angles with respect to the trailing-edge skeleton line.

The comparison of the measured aerodynamic forces and moments between the configurations of adaptive wing and conventional trailing-edge flaps demonstrates that the adaptive wing configuration exhibits both significantly higher lift coefficients at given angles of attack and substantially lower drag coefficients at given lift coefficients. This improvement in aerodynamic performance is further reflected by increased efficiencies in altering lift and pitching moment over the regarded angle-of-attack range of −10° to +30°. The adaptive wing aerodynamic potential enables also effective maneuver load alleviation.

References

[1] Hilbig H, and Wagner H. Variable wing camber control for civil transport aircraft. *Proceedings of the 15th Congress of the International Council of the Aeronautical Sciences*, Toulouse, France, ICAS-84-5.2.1, pp 107-112, 1984.

[2] Renken J H. Mission adaptive wing camber control systems for transport aircraft. *AIAA Paper 85-5006*, Oct. 1985.

[3] Greff E. The development and design integration of a variable camber wing for long/medium range aircraft. *The Aeronautical Journal*, Vol. 94, No. 939, pp 301-312, 1990.

[4] Spillmann J J. The use of variable camber to reduce drag, weight and costs for transport aircraft. *The Aeronautical Journal*, Vol. 96, No. 951, pp 1-9, 1992.

[5] Mertens J. Some important results of the technology program RaWid. *New Results in Numerical and Experimental Fluid Mechanics II, Notes on Numerical Fluid Mechanics*, Vol. 72, vieweg, pp. 315-322, 1999.

[6] Stanewsky E. Aerodynamic benefits of adaptive wing technology. *Aerospace Science and Technology*, Vol. 4, No. 5, pp 439-452, 2000.

[7] Henke R. ProHMS – Prozesskette Hochauftrieb mit multifunktionalen Steuerflächen. *Proceedings of the German Aerospace Congress 2002*, Stuttgart, Germany, DGLR-2002-094, 2002.

[8] Henke R. Forschung in Europa: Ergänzung der nationalen Arbeiten und Wegbereitung ins Produkt. *13th DGLR Symposium of STAB*, Technische Universität München, Munich, Germany, 2002.

[9] Monner H P, Breitbach E, Bein Th, and Hanselka H. Design aspects of the adaptive wing – the elastic trailing edge and the local spoiler bump. *The Aeronautical Journal*, Vol. 104, No. 1032, pp 89-95, 2000.

[10] Birkemeyer J. Widerstandsminimierung für den transsonischen Flügel durch Ventilation und adaptive Konturbeule. Deutsches Zentrum für Luft- und Raumfahrt, *Technical Report DLR-FB-99-28*, 1999.

[11] Sommerer A, Lutz Th, and Wagner S. Numerical optimisation of adaptive transonic airfoils with variable camber. *Proceedings of the 22nd Congress of the International Council of the Aeronautical Sciences*, Harrogate, UK, ICAS-2000-2.11.1, 2000.

[12] Pritschow G, and Wadehn W. Design of an adaptive wind tunnel mock-up with shape memory alloys. *Proceedings of the 8th International Conference on New Actuators,* Actuator 2002, Bremen, Germany, 2002.

[13] Müller D, and Reiners D. Adaptiver Tragflügel, Integration des Hornkonzepts in ein Landeklappensystem. *Proceedings of the German Aerospace Congress 1999*, Berlin, Germany, DGLR-JT99-048, 1999.

[14] Campanile L F, Sachau D, and Seelecke S. Ein adaptives Windkanalmodell für einen adaptiven Tragflügel. *Proceedings of the German Aerospace Congress 1999*, Berlin, Germany, DGLR-JT99-050, 1999.

[15] Recksiek M, Hoffmann M, Schmitt N, Lembcke T, and Schievelbusch B. Entwurf eines Hochauftriebssystems zur Ansteuerung multifunktionaler Steuerflächen. *Proceedings of the German Aerospace Congress 2002*, Stuttgart, Germany, DGLR-2002-098, 2002.

[16] Dargel G, Hansen H, Wild J, Streit T, Rosemann H, and Richter K. Aerodynamische Flügelauslegung mit multifunktionalen Steuerflächen. *Proceedings of the German Aerospace Congress 2002*, Stuttgart, Germany, DGLR-2002-096, 2002.

[17] Bonnema K, and Smith S. AFTI/F-111 Mission Adaptive Wing Flight Research Program. *AIAA Paper 88-2118*, May 1988.

[18] Smith S B, and Nelson D W. Determination of the aerodynamic characteristics of the mission adaptive wing. *AIAA Journal of Aircraft*, Vol. 27, No. 11, pp. 950-958, 1990.

[19] Goecke Powers S, Webb D L, Friend E L, and Lokos W A. Flight test results from a supercritical mission adaptive wing with smooth variable camber. *NASA-TM-4415*, Nov. 1992.

[20] Thornton S V. Reduction of structural loads using maneuver load control on the Advanced Fighter Technology Integration (AFTI)/F-111 Mission Adaptive Wing. *NASA-TM-4526*, Sept. 1993.

[21] Becker J, and Luber W. The role of buffeting on the structural design of Eurofighter. *AIAA Paper 2003-1889*, April 2003.

[22] Hufnagel K, and Ewald B. Force testing with internal strain gage balances, *DGLR Symposium on Cryogenic Wind Tunnel Testing*, Technische Universität München, Munich, Germany, 2001.

[23] Breitsamter C. Turbulente Strömungstrukturen an Flugzeugkonfigurationen mit Vorderkantenwirbeln. Dissertation, ISBN 3-89675-201-4, Herbert Utz Verlag Wissenschaft, 1997.